RESEARCH ARTICLE

Key Points:
- Mean value of ice water path is a poor diagnostic of cirrus radiative impact
- Both radar and lidar are needed to describe the full ice water path distribution
- Net cloud radiative effect suggests balance between cirrus and deep clouds

Cloud properties and radiative effects of the Asian summer monsoon derived from A-Train data

Elizabeth Berry[1] and Gerald G. Mace[1]

[1]Department of Atmospheric Science, University of Utah, Salt Lake City, Utah, USA

Abstract Using A-Train satellite data, we investigate the distribution of clouds and their microphysical and radiative properties in Southeast Asia during the summer monsoon. We find an approximate balance in the top of the atmosphere (TOA) cloud radiative effect, which is largely due to commonly occurring cirrus layers that warm the atmosphere, and less frequent deep layers, which produce a strong cooling at the surface. The distribution of ice water path (IWP) in these layers, obtained from the 2C-ICE CloudSat data product, is highly skewed with a mean value of $440 \, \mathrm{g \, m^{-2}}$ and a median of $24 \, \mathrm{g \, m^{-2}}$. We evaluate the fraction of the total IWP observed by CloudSat and CALIPSO individually and find that both instruments are necessary for describing the overall IWP statistics and particularly the values that are most important to cirrus radiative impact. In examining how cloud radiative effects at the TOA vary as a function of IWP, we find that cirrus with IWP less than $200 \, \mathrm{g \, m^{-2}}$ produce a net warming in the study region. Weighting the distribution of radiative effect by the frequency of occurrence of IWP values, we determine that cirrus with IWP around $20 \, \mathrm{g \, m^{-2}}$ contribute most to heating at the TOA. We conclude that the mean IWP is a poor diagnostic of radiative impact. We suggest that climate model intercomparisons with data should focus on the median IWP because that statistic is more descriptive of the cirrus that contribute most to the radiative impacts of tropical ice clouds.

1. Introduction

Clouds and precipitation remain one of the largest sources of uncertainties in climate projections [*Andrews et al.*, 2012; *Li et al.*, 2013; *Su et al.*, 2013]. To the first order, the general circulation fundamentally determines the distributions of clouds and cloud properties. Clouds, however, feed back on the atmospheric circulation through their effects on surface and atmospheric heating via radiation and latent heat release in precipitation [*Stephens*, 2005]. The radiative and latent heating by clouds and precipitation are, therefore, not only important in terms of energy balance but also because of their coupling to the large-scale dynamics.

Documenting the vertical distribution of cloud occurrence and cloud properties and the resulting heating and cooling profile of the atmosphere due to clouds is important for understanding cloud forcing and feedbacks. Several previous studies have used observations to derive cloud heating rates. Early examples that looked at cloud radiative effects were based on the International Satellite Cloud Climatology Project [*Rossow and Lacis*, 1990; *Chen et al.*, 2000; *Zhang et al.*, 2004]. Other studies are based on data collected at Atmospheric Radiation Measurement Program ground sites [*Mather et al.*, 2007; *Mace and Benson*, 2008; *Mather and McFarlane*, 2009; *Powell et al.*, 2012]. More recent studies use active space-based remote sensors to estimate profiles of cloud radiative and latent heating rates. These studies utilize the precipitation radar on the Tropical Rainfall Measurement Mission (TRMM) satellite [*Jensen and Del Genio*, 2003; *Schumacher et al.*, 2008] and cloud radar on CloudSat [*L'Ecuyer et al.*, 2008; *Mace*, 2010; *Stephens et al.*, 2012; *Haynes et al.*, 2013; *Henderson et al.*, 2013]. Ongoing work seeks to reconcile the different cloud radiative effects estimates [*Protat et al.*, 2014] and use the derived cloud radiative heating rates to help evaluate models [*McFarlane et al.*, 2007].

New information about the vertical distribution of clouds from satellites became available in 2006, when the CloudSat and Cloud-Aerosol Lidar and Infrared Pathfinder Satellite Observations (CALIPSO) satellites were added to the A-Train [*L'Ecuyer and Jiang*, 2010]. CloudSat features a 94 GHz Cloud Profiling Radar (CPR) [*Im et al.*, 2006] and provides measurements of radar reflectivity profiles. CALIPSO features the Cloud-Aerosol Lidar with Orthogonal Polarization (CALIOP) [*Winker et al.*, 2007] that provides measurements of attenuated backscatter and depolarization in two channels. The synergy of these active remote sensors along with the near coincident measurements from the other A-Train sensors provides unique independent information about the vertical distribution of clouds and cloud properties that can be utilized in combination with passive remote sensor data for deriving cloud properties [*Austin et al.*, 2009; *L'Ecuyer et al.*, 2008].

Of particular interest in this study are high clouds given that atmospheric ice properties have not been well constrained observationally and are known to have broad differences across the leading climate models [*Eliasson et al.*, 2011]. *Li et al.* [2012] found factors of 2–10 differences in the annual mean cloud ice water path (IWP) among different observationally based data sets and general circulation models (GCMs). *Jiang et al.* [2012] found that modeled mean cloud water contents over the tropical oceans range from 3% to a factor of 15 of observations in the upper troposphere and 40% to a factor of 2 of the observation in the lower and middle troposphere, revealing that the spread and error in mean IWC is much larger than the spread and error in mean LWC among GCMs. These uncertainties would affect the vertical distribution of radiative heating within the atmosphere. While the shortwave fluxes at the top of atmosphere (TOA) are sensitive to the IWP, the longwave radiation would depend primarily on the temperature near cloud top for optically thick layers and essentially decouple the radiation balance from the IWP distribution. This may explain why GCMs have broad difference in mean IWP, but still reach consensus with TOA radiation. There are alternative explanations, however.

A study by *Soden and Vecchi* [2011] found a consistent response of strong positive high cloud feedback to warming among GCMs. As explained by *Zelinka and Hartmann* [2010], because tropical convection tends to detrain at consistently higher heights and colder temperature as the climate warms, the infrared (IR) forcing of tropical anvils becomes increasingly strong. An increasingly positive forcing with warming is the definition of a positive feedback (also known as, the Proportionately High Anvil Temperature hypothesis [*Zelinka and Hartmann*, 2010]). The consistency in feedback (i.e., the change in forcing) from wildly divergent cloud properties is interesting and implies that either the relative magnitudes of the radiative forcing differences within the multimodel ensemble must be compensating in some manner or the feedback is insensitive to the mean ice water path in the tropical upper troposphere. Our ultimate goal is to ascertain to what extent climate models are representing actual radiative forcing by cirrus in the atmosphere. A first step, and the purpose of this paper, is to document through observations the means by which clouds generally and high clouds in particular radiatively heat the real tropical atmosphere. Ultimately, the question we wish to address is what type of cirrus is most important to the radiative heating in the upper troposphere because it is the changes in the heating of these clouds with radiative forcing that determine the positive feedback tropical ice clouds have on the climate system.

Therefore, in this study we seek to gain a better understanding of the relationship between the IWP, the cloud radiative effect (CRE), and the cloud radiative heating using observations from the A-Train. In particular, we examine how the radiative heating by high clouds is distributed as a function of IWP in a domain centered on the Southeast Asian Summer Monsoon that is dominated by a wide variety of cirrus ranging from thick precipitating anvils to thin isolated cirrus. The techniques used in this study build upon previous work by *Deng et al.* [2010] and *Mace* [2010, hereinafter M10], and summaries of these methods and additional methodological material are provided in section 2. Section 3 summarizes the cloud occurrence frequency and IWP climatology for the region. Section 4 presents the statistics of cloud microphysical properties, heating rates, and radiative effects. A summary of the main findings is given in section 5.

2. Data and Methodology

Our objectives require us to have a fairly complete description of the physical and thermodynamic state of the atmosphere along the CloudSat/CALIPSO tracks. This includes profiles of temperature and water vapor as well as the vertical distribution of cloud radiative properties. Deriving radiative properties from remote sensing data remains severely underconstrained because there are many more free parameters than independent measurements that are sensitive to the cloud microphysical properties. Therefore, simplifying assumptions must be applied to algorithms that operate on measurements collected by the A-Train remote sensors. Our basic philosophy is to consider the A-Train as a single synergistic measurement platform. Therefore, we combine multiple data streams to describe the cloud occurrence profile and to derive the cloud microphysical properties.

The CloudSat datasets known as the Geometrical Profiling Product (GEOPROF) [*Marchand et al.*, 2008; *Mace et al.*, 2007], the Radar-Lidar Geometrical Profiling Product (RL-GEOPROF) [*Mace et al.*, 2009; *Mace and Zhang*, 2014] and the European Centre for Medium-Range Weather Forecasts (ECMWF) Auxiliary product [*Partain*, 2004] provide the principle descriptions of the atmospheric state that we require. While GEOPROF provides a cloud mask, radar reflectivity from the CPR, and gaseous
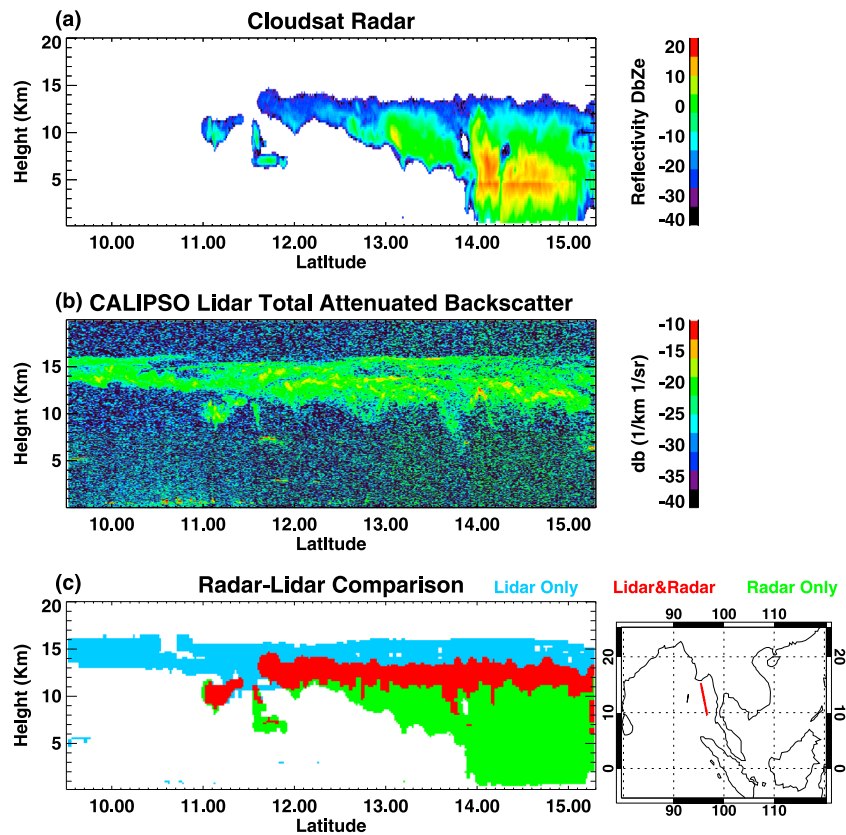
Figure 1. A typical cloud scene in the Southeast Asia analysis region observed in the afternoon on 18 August 2008. (a) CloudSat radar reflectivity, (b) CALIPSO lidar backscatter, and (c) the combined radar-lidar cloud mask. The red line on the map shows the location of this cloud scene.

attenuation of the radar beam, the GEOPROF-LIDAR product combines cloud masks of the CPR and CALIOP. The ECMWF Auxiliary product provides thermodynamic state variables that have been interpolated to each radar resolution volume. Figure 1 shows a typical cloud scene from Southeast Asia. Figure 1a displays the CloudSat radar reflectivity (resolution ~ 1.4 km across track and 2.1 km along track), Figure 1b displays the CALIOP 532 nm attenuated backscatter (horizontal resolution = 333 m below 8.2 km and 1 km above 8.2 km), and Figure 1c demonstrates how the CPR and CALIOP are combined to create the cloud mask in GEOPROF-LIDAR [*Mace et al.*, 2009; *Mace and Zhang*, 2014]. We also use Moderate Resolution Imaging Spectroradiometer (MODIS) visible optical depths from the MODIS Level 2 Joint Atmosphere Product (5 km resolution) [*Platnick et al.*, 2003], liquid water paths derived from the Advanced Microwave Scanning Radiometer–Earth Observing System (AMSR-E) microwave brightness temperatures (13 km resolution) [*Wentz and Meissner*, 2000], and solar and IR irradiances derived from the Clouds and the Earth's Radiant Energy System (CERES) (20 km resolution) [*Wielicki et al.*, 1998] in the retrieval of cloud properties.

Cloud microphysical and radiative properties and profiles of radiative fluxes along the CloudSat track are derived using a suite of techniques that were initially developed and applied to a similar suite of ground-based remote sensors [*Mace et al.*, 2006; *Mace and Benson*, 2008]. The modifications that we have made for specific application to the A-Train are described in M10. Because our goal is to examine the radiative heating profiles, the algorithms are comprehensive in that liquid, and ice cloud property profiles are estimated. The change we make in this study is to replace the ice-phase retrieval results in M10 with a new CloudSat standard data product known as 2C-ICE. To derive vertically resolved ice water content, ice effective radius, and extinction coefficient profiles, 2C-ICE combines the CPR and CALIOP profiles of attenuated backscatter [*Deng et al.*, 2010, 2013]. For the mixed phase region where the lidar is
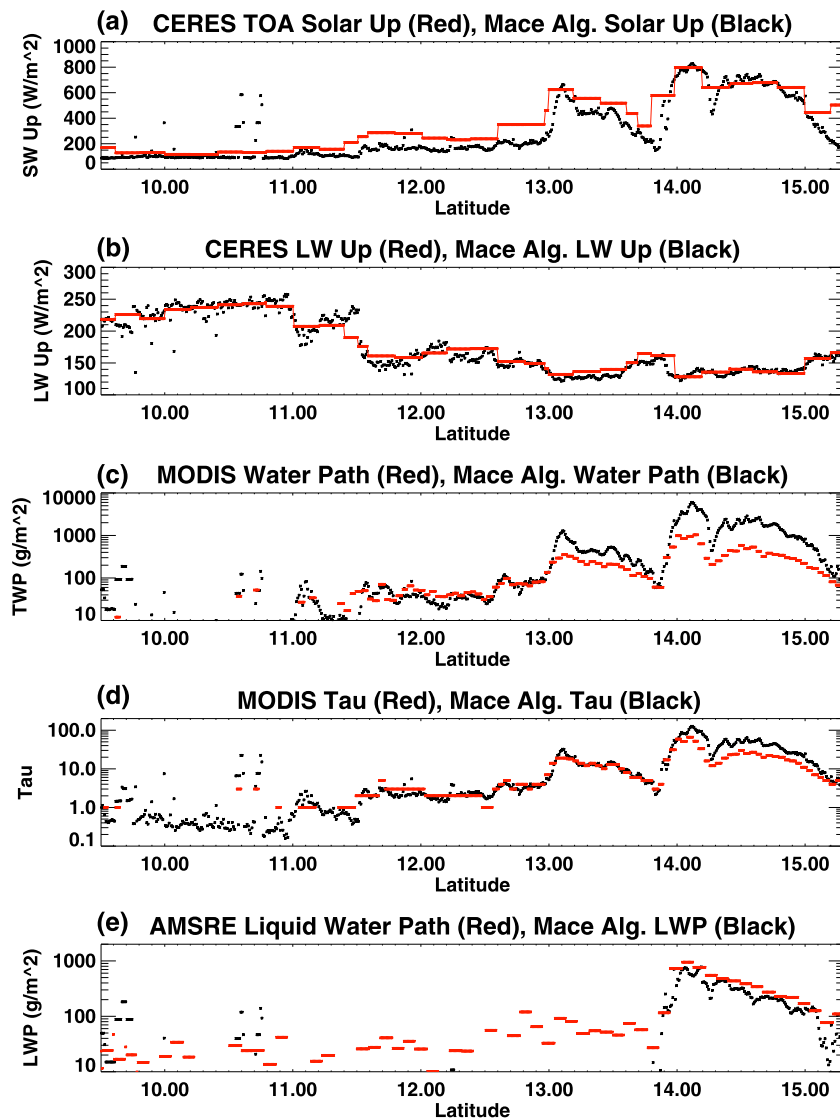
Figure 2. The retrieved microphysics and radiative fluxes for the typical cloud scene shown in Figure 1. (a) Reflected solar at TOA, (b) outgoing longwave at TOA, (c) total water path, (d) optical depth, and (e) liquid water path. Our retrieved values (in black) are compared to other retrievals for each quantity.

usually attenuated, 2C-ICE treats the layer as only containing the ice phase and performs a radar-only retrieval for temperatures less than −4°C.

Once the microphysical properties have been determined, we calculate the radiative properties. For liquid water, we use the *Slingo* [1989] and *Kiehl et al.* [1998] parameterizations for the shortwave and longwave radiative properties, respectively. For ice, we use the *Fu* [1996] and *Fu et al.* [1998] parameterization for the shortwave and longwave radiative properties, respectively. The radiative properties are then used to calculate the profiles of shortwave and longwave radiative fluxes with the two-stream radiative transfer model described by *Toon et al.* [1989] with the *k*-distribution method and correlated-*k* assumptions described by *Kato et al.* [1999, 2001] for the solar spectrum and by *Mlawer et al.* [1997] for the infrared spectrum.

Figure 2 shows the retrieved microphysics and radiative fluxes for the cloud scene presented in Figure 1. We find considerable variability along this curtain as the scene transitions from a thin cirrus anvil at 10° latitude to deep convection at 15° latitude. The deep convective cloud is reflecting nearly 800 W m^{-2} of solar radiation, compared to the thin cirrus anvil, which is only reflecting about 100 W m^{-2} (Figure 2a). We also see that the

outgoing longwave radiation is greatly reduced by the deep convection with only 80 W m^{-2} escaping to space compared to 250 W m^{-2} for the thin cirrus (Figure 2b). The total water path ranges from 5 g m^{-2} in the thin cirrus, up to several kg m^{-2} in the deep convection (Figure 2c). Our derived values generally compare well to other data sets like CERES radiative fluxes and MODIS Level 2 cloud properties, which are shown in red in Figure 2. The largest differences are found in total water path (TWP) and visible optical depth (Figures 2c and 2d, respectively) for the portion of deep convective cloud located between 14 and 15° latitude. While the differences between MODIS (TWP ~ 400 g m^{-2} and τ ~ 20) and our retrieval (TWP ~ 2000 g m^{-2} and τ ~ 60) are large in this scene, it is not surprising given that the uncertainties in each retrieval are also large for a deep convective case like this. In addition, the retrievals are fundamentally different, with MODIS TWP being inferred from visible reflectances that tend to asymptote at high optical depths, while our algorithm infers TWP from active measurements that are sensitive to the vertical distribution of microphysical properties. However, given the uncertainties, we can only be confident that the optical depths of this vertically extended cloud are certainly much larger than 20.

Errors in the microphysical retrieval algorithm results translate into errors in the radiative property profiles and ultimately to the radiative heating rates via errors in the fluxes. It is certainly challenging to track the errors from microphysical retrievals to heating rates. Using comparisons with in situ data and comparisons to other cloud property retrieval algorithm results (Aqua-MODIS cloud product, AMSR-E liquid water path product, and the radar-only CloudSat cloud water content product), M10 shows that uncertainty in LWC in shallow clouds is on the order of 50% and that characteristic error in LWP for shallow clouds would be on the order of 40% assuming random, uncorrelated, and unbiased error statistics. Errors in the 2C-ICE cloud properties have been evaluated by comparing with 17 in situ flight legs in cirrus under the A-Train during the Small Particles in Cirrus campaign [*Deng et al.*, 2013]. Accounting for uncertainties in the measurements and forward models, we expect that any individual retrieval to have errors in IWC and effective radius on the order of 70% and 40%, respectively [*Deng et al.*, 2013]. Comparisons with in situ data suggest that the errors are largely unbiased and appear to converge on RMS differences of 12% for IWC and 5% for effective radius. Following the error analysis presented in Appendix C of M10, errors in the cloud radiative effects are assumed to be on the order of 5–10 W m^{-2} for multimonth averages. To obtain the error in the cloud radiative heating rate, we calculate the variance in cloud heating rate, divide by the number of independent samples, and take the square root, as in M10. We consider every 50 CloudSat profiles (approximately every 100 km along track) to be an independent sample. Given that the uncertainties scale by the number of independent samples, the errors in cloud heating for a specific cloud type depend on the frequency of occurrence of that given cloud type. We find cloud type-specific heating rate errors to be between 1 and 2 K d^{-1}. Given the magnitudes of the cloud radiative effects and the cloud radiative heating rates presented below, these uncertainties are substantial but do allow us to extract limited information from these results.

3. Cloud Properties in Southeast Asia

For this study we focus on a 30° × 40° region over Southeast Asia [5°S–25°N, 80°E–120°E] for the months of August and September of the years 2007 and 2008. The hallmark of the summer monsoon in Southeast Asia is low-pressure area that develops over the warm continent, accompanied by onshore winds that transport moisture toward the land. At upper levels, the dynamics of the region are characterized by an anticyclonic circulation that ventilates the convergence associated with the low-level monsoon flow. The deep convection that develops during the summer monsoon is associated with reduced (approximately < 200 W m^{-2}) outgoing longwave radiation [*Park et al.*, 2007] and climatologically large amounts of precipitation, in excess of 1200 mm in the Bay of Bengal over a 4 month period [*Hoyos and Webster*, 2007]. Particularly over the Bay of Bengal, wind shear exists between the easterly jet at upper levels and the northwesterly flow at the surface [*Houze et al.*, 2007], which influences the characteristics of the cirrus anvils.

Several studies have examined the properties of clouds in Southeast Asia. *Houze and Churchill* [1987] made an interesting observation that the monsoon clouds sampled there during an airborne campaign contained an abrupt change in phase and were virtually liquid free above the freezing point. *Zuidema* [2003] used infrared satellite imagery to study the lifecycle of convective clouds over the Bay of Bengal and found that the most common propagation direction is to the southwest and that these oceanic cold-topped clouds develop late in the evening and dissipate after sunrise, with the larger systems lasting until the afternoon. More recently, using
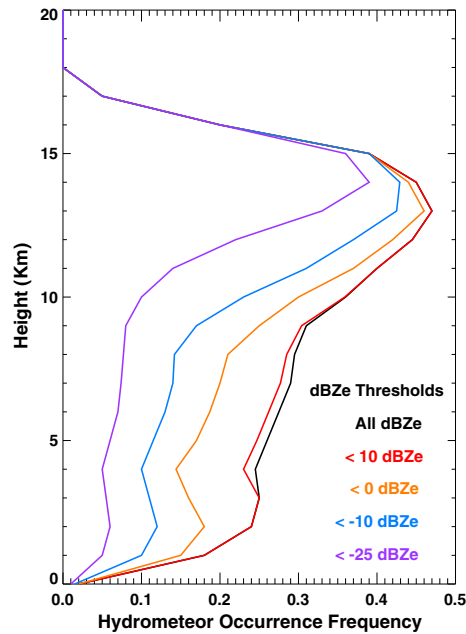
Figure 3. Hydrometeor occurrence frequency as a function of height from the CloudSat-CALIPSO merged data set for the monsoon season in the Southeast Asia study region. The radar reflectivity thresholds indicate the occurrence frequency for all observations that have radar reflectivity below the threshold value.

CloudSat and TRMM data, *Cetrone and Houze* [2009] discovered that anvil clouds in the Bay of Bengal are deeper with lower base heights compared to anvils in West Africa and the Maritime Continent. They also noted that lifted parcels in the Bay of Bengal exhibit positive buoyancy throughout the depth of the troposphere. A more extensive study by *Romatschke and Houze* [2011] used 8 years of TRMM data to specifically examine precipitating convective systems in the South Asian Monsoon. They found that rainfall in the Bay of Bengal is dominated by the largest size systems ($>$44,000 km^{-2}), which have a convective fraction of 40% and a stratiform fraction of 56%. However, stratiform precipitation was more common over the open water in the central Bay of Bengal, while convective precipitation was more common near the coast of Myanmar. They also noted that these large systems over the Bay of Bengal exhibit a pronounced diurnal cycle, with a minimum occurrence during the evening and a maximum occurrence around midday.

As derived from the Radar-Lidar Geometrical Profile Product (RL-GEOPROF) [*Mace et al.*, 2009; *Mace and Zhang*, 2014], Southeast Asia during the monsoon season is one of the cloudiest places on Earth, with hydrometeor layer occurrence frequency along the CloudSat track exceeding 85%. Figures 3 and 4, compiled from the merged CloudSat-CALIPSO data sets, document the geometric distribution of hydrometeor layers in the study region during the two summer monsoon seasons under scrutiny. The predominance of layers based in the upper troposphere is clearly evident from these statistics, and we find that a large fraction of layers based in the upper troposphere (above 6 km) are geometrically thicker than 3 km. Cirrus based in the Tropopause Transition Layer (above 14 km) are primarily geometrically thin (less than 1.5 km) and are predominantly observed only by CALIPSO as discussed below. However, we also find a distinct peak of hydrometeor layers with tops above 14 km and thicknesses from 3 to 6 km. These thicker layers are likely composed primarily of anvil cirrus recently associated with deep convection. The hydrometeor layers in the upper troposphere tend to be composed primarily of volumes with radar reflectivity less than -25 dBZ_e although the fraction of volumes with higher reflectivity increases systematically from higher to lower heights. For instance, above 14 km more than 85% of the observed volumes have reflectivity less than -25 dBZ_e, while at 10 km, only one third of the observed volumes have
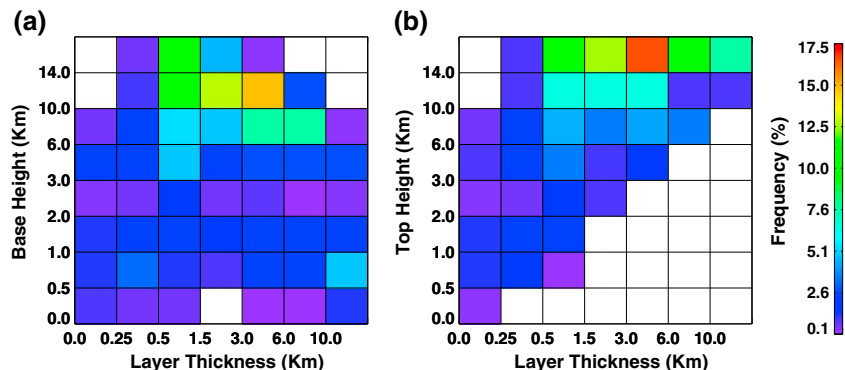
Figure 4. (a) Hydrometeor layer base and (b) hydrometeor layer top by layer thickness histograms for the monsoon season in the Southeast Asia study region compiled from the 2007–2008 RL-GEOPROF data.
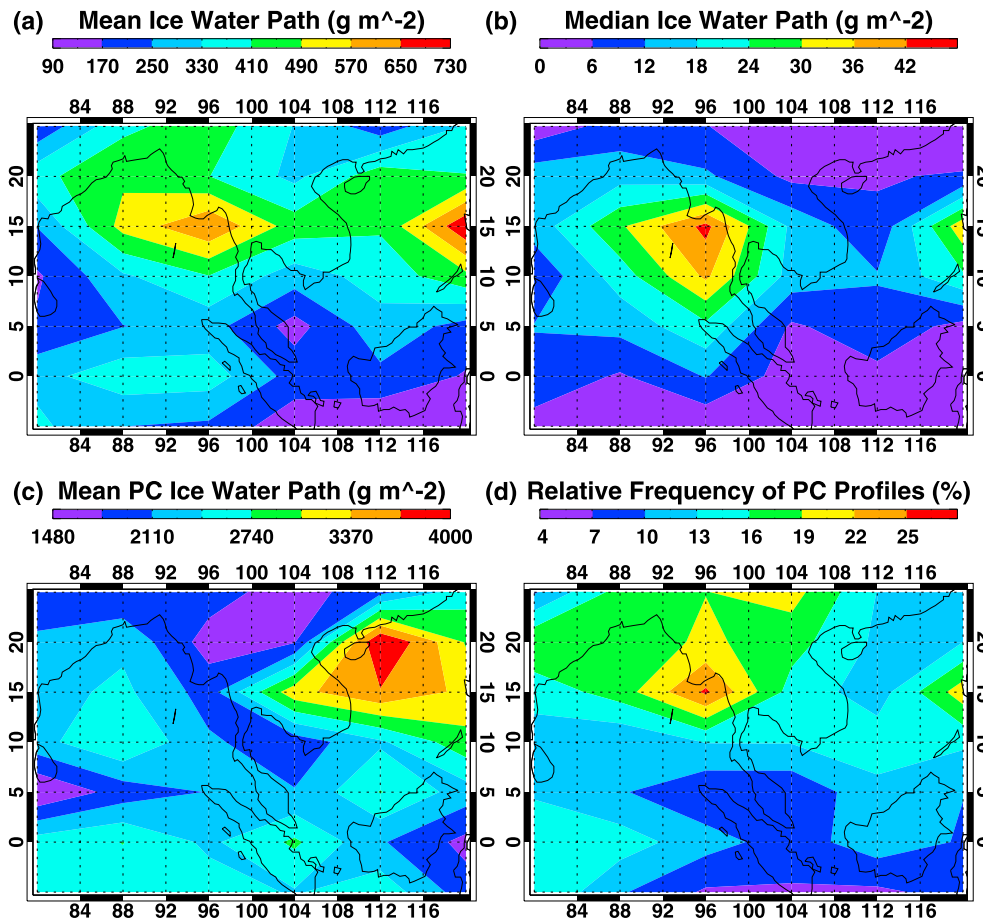
Figure 5. Geographical distribution of ice water path for August–September 2007–2008. (a) Mean IWP, (b) median IWP, (c) mean precipitating/convective IWP, and (d) the percentage of precipitating/convective profiles, relative to the total number of profiles that contain ice.

reflectivity less than −25 dBZ_e. We interpret this structure in reflectivity statistics as being the result of differential settling of larger particles in precipitating anvils.

Moving down from the upper troposphere, we find a local maximum of geometrically thin layers between 3 and 6 km that are likely middle level clouds that tend to occur near the freezing level. These statistics regarding midlevel layers are almost certainly an underestimate because the ubiquitous high clouds block these typically low dBZ_e layers from view by the CALIPSO lidar. Much of the hydrometeors in the middle troposphere in this regions are parts of deeper layers and tend to have higher reflectivity—nearly one third of all hydrometeor volumes have radar reflectivity in excess of 0 dBZ_e indicative of precipitation.

Hydrometeor layers based in the lower troposphere have weak maxima at the thinnest and thickest layer thicknesses with a population of layers that extend across all thickness bins. This results in the local maximum in the vertical occurrence frequency seen near 3 km in Figure 3. Apparently shallow boundary layer cumulus are rarely observed in this region by the A-Train although some care must be used in interpreting these findings because many of these clouds would be below the sensitivity of the CloudSat radar and be blocked from view by CALIPSO due to higher hydrometeor layers. The thicker layers based in the lower troposphere would likely be precipitating (at least weakly) and be within the sensitivity threshold of CloudSat. Deep layers represent a significant fraction of the overall data set and are indicated in Figure 4 by the local maximum with the lowest bases and highest tops with the largest layer thicknesses. While some fraction of these layers would be deep convection, many if not most of them would be classified as regions of stratiform rain associated with convective complexes [*Romatschke and Houze*, 2011]. An example of a region of stratiform rain, indicated by the radar bright band near 5 km, can be seen in Figure 1 between 14° and 15°N.
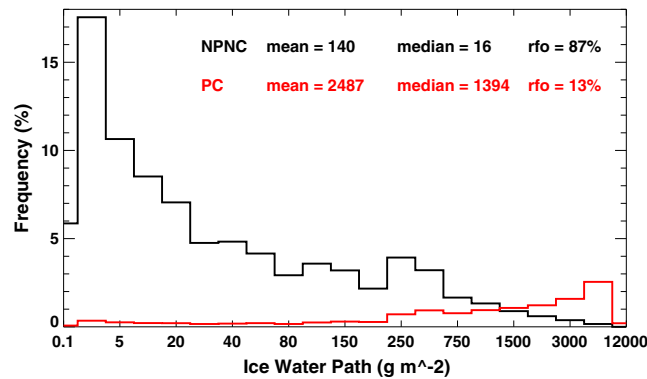
Figure 6. Frequency distribution of ice water path for nonprecipitating and nonconvective profiles (shown in black) and precipitating/convective profiles (shown in red).

3.1. Ice Water Path Statistics

Knowing the distribution of IWP is fundamental to understanding the energetic balance of the tropical atmosphere. The active remote sensors in the A-Train provide a unique perspective that allows us to explore the IWP statistics in detail using the 2C-ICE data. As discussed earlier, previous studies have focused on the mean value of IWP and found drastic differences among various data sets and between data sets and models. In our analysis region, we find domain-wide mean and median IWP to be $440 \, g \, m^{-2}$ and $24 \, g \, m^{-2}$, respectively, in approximate agreement with the observational findings of *Li et al.* [2012]. The plan view of IWP statistics (Figures 5a and 5b) shows regional maxima centered south of Myanmar and another at the eastern boundary of our analysis domain near the Philippines. These maxima have mean and median values of IWP in excess of $600 \, g \, m^{-2}$ and $40 \, g \, m^{-2}$, respectively. Most of the analysis region demonstrates mean IWP in excess of $300 \, g \, m^{-2}$ while the larger median values tend to be more concentrated over the Andaman Sea west of Thailand.

The large differences between the mean and median IWP values suggest a highly skewed distribution of IWP, and this is confirmed in Figure 6. Following the approach taken by recent investigators [*Waliser et al.*, 2009; *Jiang et al.*, 2012; *Li et al.*, 2013] we classify the profiles based on whether they appear to be precipitating or convective (PC) or nonprecipitating and nonconvective (NPNC) using the classification scheme described by *Wang et al.* [2011] known as 2B-CLDCLASS-LIDAR—one of the standard data products available in the CloudSat data archive. Maps of the distribution of PC profiles are shown in Figures 5c and 5d. The mean values of IWP are primarily determined by rarely occurring precipitating/convective events while the majority of ice layers, represented best by the median of the IWP distribution, are derived from more frequent and widely distributed layers of moderate or small water path. The precipitating/convective events that dominate the mean IWP occur in the heavily raining stratiform areas of mesoscale convective complexes where ice crystal properties are unknown, the radar scattering is likely to be non-Rayleigh, and attenuation and multiple scattering are likely important to the radar reflectivity measurements. The CloudSat ice water retrieval algorithm [*Austin et al.*, 2009] used by *Waliser et al.* [2011] and *Jiang et al.* [2012] as well as the 2C-ICE results have not been critically evaluated in regions of convection or heavy stratiform rain associated with mesoscale convective complexes and the error characteristics of the retrievals are unknown. So while we know the ice water paths are very large in these precipitating/convective profiles, attaching significance to large IWP values in the tail of the distribution in Figure 6 that significantly influence the IWP mean is a risky undertaking.

An important consideration when evaluating the validity of the statistics in Figures 5 and 6 is the source of information. The 2C-ICE algorithm combines measurements from both the CPR and CALIOP and therefore has the best error characteristics in the
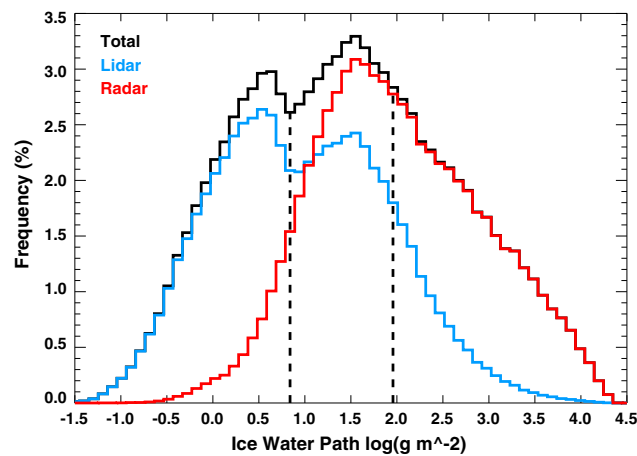
Figure 7. Histogram of 2C-ICE ($n = 671,792$ profiles) total ice water path (black line), and the portion of ice water path observed by just the lidar (blue line) and just the radar (red line). The black dashed lines mark the upper and lower tercile.

Table 1. Cloud Type Definitions Based on Cloud Layer Top Height and Cloud Thickness[a]

Cloud Type	Cloud Top Height	Cloud Thickness	RFO
TTL Cirrus	> 14 km	< 3 km	11%
Thin Cirrus	10–14 km	< 3 km	13%
Thick Cirrus	> 10 km	3–6 km	23%
Deep Layers	> 10 km	> 6 km	34%
Mid-level Clouds	6–10 km	< 10 km	10%
Low Clouds	< 6 km	< 6 km	9%

[a]The relative frequency of occurrence for each cloud type is listed in the last column.

region where the measurements overlap. Typically, as illustrated in Figure 1, the tops of many ice cloud layers are composed of cloudy volumes not detectable by the CPR and the bases of many thicker ice cloud layers are not detectable by CALIOP. The 2C-ICE retrieval then reverts to a radar-only or a lidar-only approximation, and the uncertainty of the retrieved ice cloud properties increases significantly [*Deng et al.*, 2013]. Figure 7 shows the distribution of IWP as in Figure 6 except re-rendered in semi-log space. For each log(IWP) bin in the distribution, we note the fraction of ice water path from the portions of the layers that were detected by CALIOP and the portions of the layers that were detected by the CPR, keeping in mind that there is some overlap between them. This allows us to see that the distributions of IWP were only one of the instruments available and in what IWP range the 2C-ICE retrievals are most reliable.

When viewed in semi-log space, we find that the IWP distribution is bimodal with a primary peak around 30 g m^{-2} where both the CPR and CALIOP contribute and a secondary peak around 3 g m^{-2} where the CPR is insensitive and the information comes primarily from CALIOP. Evidence for this bimodal distribution is also seen in Figure 4. The maximum in occurrence for thin layers based above 10 and 14 km is primarily contributing to the small IWP mode in Figure 7 while the geometrically thicker layers contribute to the rest. By splitting the IWP distribution into terciles, we find that the lower tercile of the ice water path values fall below 6 g m^{-2} and are composed primarily of layers observed only by CALIOP. The upper tercile of the ice water path values are greater than 79 g m^{-2} and observed primarily by the CPR. At an ice water path of 10 g m^{-2}, we find the crossover between CALIOP and CPR where the instruments would separately observe the same fraction (about 75%) of the combined IWP. An example can be seen in Figure 1 near 13°N where most of the cloud layer is observed by CALIOP, while a small portion near cloud base is observed only by the CPR. The greatest synergy in the instruments, and therefore the best error characteristics in 2C-ICE, is found in the middle tercile of the log(IWP) distribution that includes the median IWP.

Therefore, because the uncertainties in the IWP events that tend to dominate the IWP mean are unknown, and because the median IWP better characterizes the nature of the IWP distribution and is derived primarily from ice cloud layers for which the synergy between the instruments is optimized, it seems that the median IWP is a more meaningful measure of central tendency to describe the IWP distribution in this region.

4. Cloud Radiative Effects

The radiative effects of clouds on the surface, atmosphere, and TOA depend to first order the distribution of cloud layers in the vertical profile and secondarily on the statistics of the microphysical properties of those layers. To investigate how the cloud vertical structure influences the radiative heating profile, we consider six hydrometeor layer types that are defined by layer top height and layer geometrical thickness (Table 1) with their relative frequencies of occurrence (RFO) listed in Figures 8 and 9 along with their bulk water paths and derived heating profiles. To isolate the heating due to clouds, the cloud radiative heating is calculated as the difference between the all-sky heating and the clear-sky heating. We choose these categories from subjective criteria that correspond to what we interpret to be either specific genre of clouds and/or specific layer types that have significantly different influences on the radiative heating budget of the profile. We note that the Low and Midlevel Clouds present a challenge to the A-Train sensors. Because of extensive optically thick high clouds, many Low and Midlevel layers are not observed by the CALIOP due to attenuation by higher clouds. For the CloudSat CPR to detect them, their tops must be higher than 1 km and have a radar reflectivity in excess of −30 dBZ_e. We also must note that as discussed above, the uncertainty in the radiative heating profiles is considerable allowing only the broadest interpretations of the results.
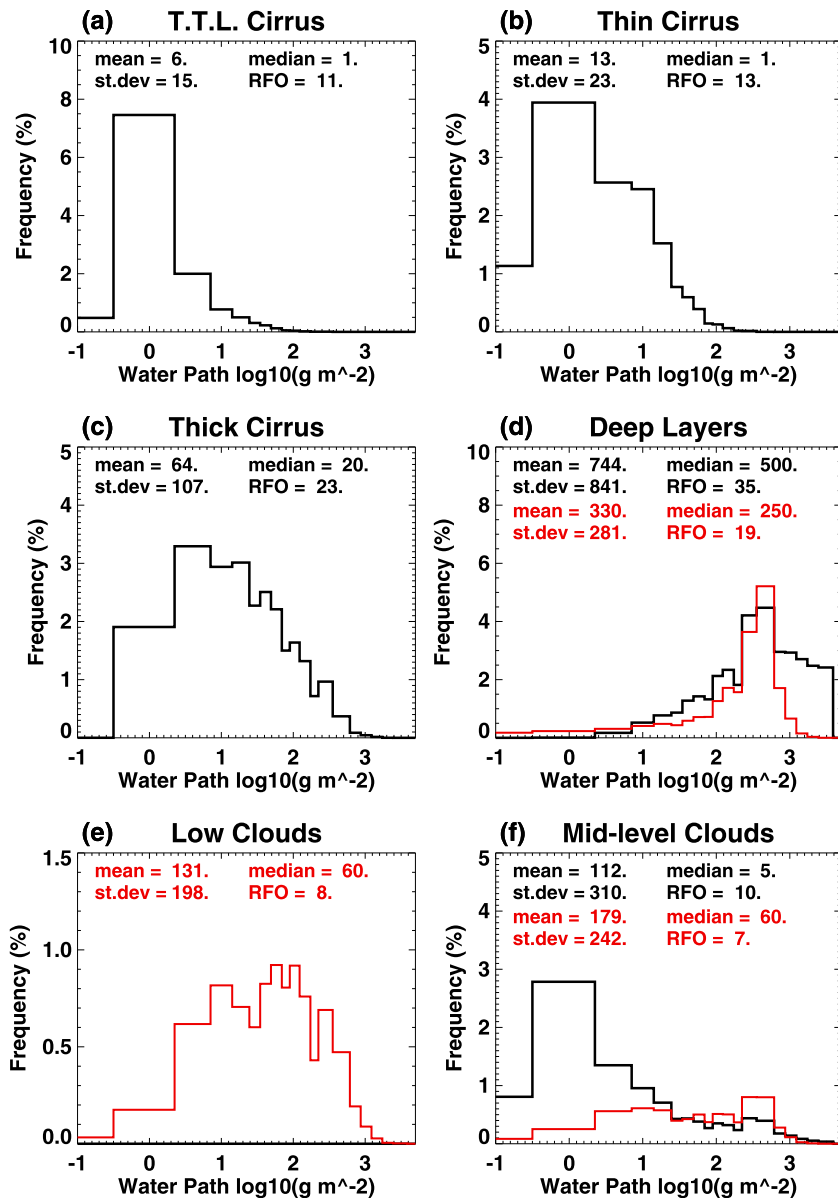
Figure 8. (a–f) Frequency distribution of ice water path (shown in black) and liquid water path (shown in red) for each cloud type. The mean, median, and standard deviation of the distributions are noted in g m^{-2}. Relative to all cloud profiles, 92% contain ice and 34% contain liquid.

The frequency distributions of the bulk water paths, shown in Figure 8, tend to be strongly skewed—especially for the cirriform layer types. As cirrus thicken geometrically and optically, their influence on the tropospheric heating structure broadens over a deeper layer. TTL cirrus, which have a relatively lower RFO compared to elsewhere in the Western Pacific and Indian Oceans [*Schwartz and Mace*, 2010], primarily influence the heating above 14 km (Figures 8a and 9a). These layers tend to be sufficiently tenuous (>90% of the IWP < 10 g m^{-2}) so they heat in the IR throughout their depth with only a small amount of solar heating. The peak heating occurs near 14 km and extends into the TTL to near 17 km. Their influence tends to become negligible below about 11 km. The Thin Cirrus category tends to have a deeper impact on the troposphere with a net heating profile that, while peaking near 2 K d^{-1} at 12 km, extends to near the top of the boundary layer. The IR heating in this layer is about a factor of 2 larger than the solar heating. The solar heating asymptotes to near zero below 10 km while the IR heating remains positive due to emission from cloud base. Even though the bases of these layers remain very cold, their presence is sufficient to induce a warming effect on the middle troposphere.
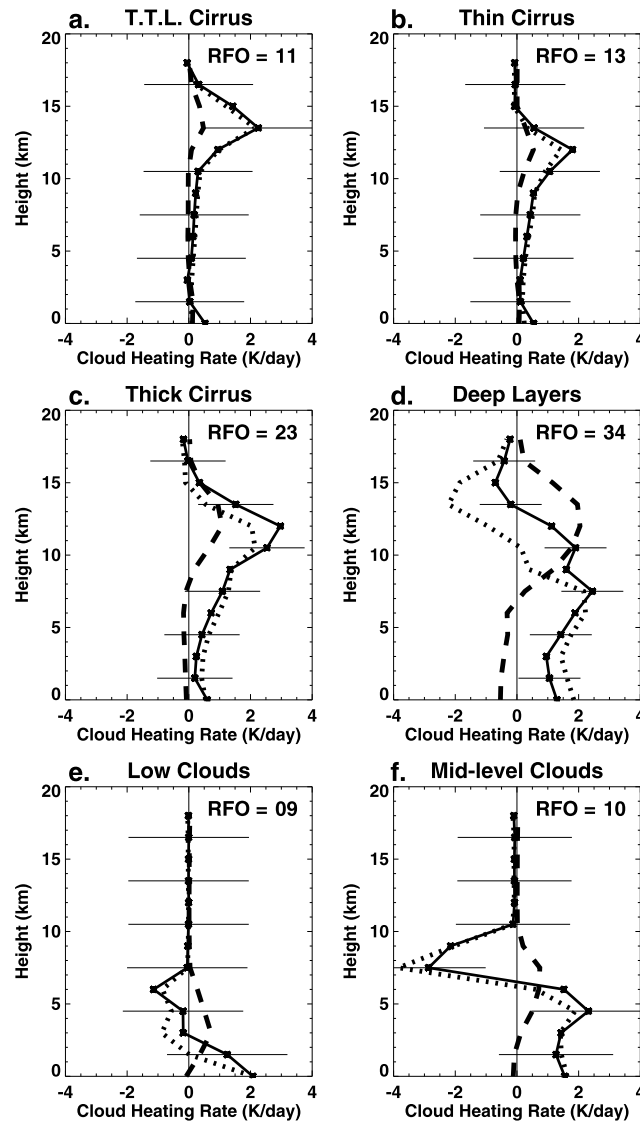
Figure 9. Mean solar (dashed), infrared (dotted line), and net (solid line) cloud heating rates for each cloud type. The net heating rate uncertainty and relative frequency of occurrence are shown for each cloud type.

Thick Cirrus on the other hand have the strongest net heating effect (~3.5 K d^{-1}). With a median IWP near 20 g m^{-2}, the typical Thick Cirrus cloud remains optically thin and tends to heat in both the IR and solar throughout their layer depth where solar heating become substantial and exceeds the IR heating above 13 km. Thick Cirrus extend a heating signature throughout the troposphere due to emission.

Deep Layers, Midlevel Clouds, and Low Clouds all tend to demonstrate net cooling near their layer tops and net heating below. Of these, Deep Layers are the most commonly observed by the A-Train and tend to have very high TWP with median values in the 750 g m^{-2} range. The strong IR warming within Deep Layers peaks near 2 K d^{-1} at 7 km. Below 7 km, IR warming is slightly mitigated by solar cooling. This solar cooling is due to the albedo of these layers, which causes solar flux that would have been absorbed in the middle and lower troposphere to be reflected to space. Near the tops of Deep Layers, the IR cooling and solar heating tend to cancel near 13 km. Midlevel Clouds, which include deeper congestus-type clouds, have a median TWP near 300 g m^{-2}. These Midlevel layers demonstrate the strongest IR cooling near 8 km, in excess of 3 K d^{-1}, while the IR heating peaks at 2 K d^{-1} near 5 km and extends to the surface. Low-Level Clouds, with median LWP near 60 g m^{-2}, demonstrate a shallow cooling and heating couplet below 7 km. Interestingly, the column-integrated net heating for Low and Midlevel Clouds is close to zero, owing to a balance between the longwave cooling found near cloud top and the solar absorption and downwelling IR below cloud top.

The overall net heating radiative heating profile (Figure 10c) demonstrates unambiguous heating throughout the column. The peak in net cloud heating approaching 1.5 K d^{-1} between 10 and 12 km and is largely due to the addition of positive IR heating from cirrus and positive solar heating by Deep Layers. The heating becomes neutral near 14 km where IR cooling and solar heating tend to balance. This profile of heating is determined primarily as a combination of the net heating profiles of the three high cloud types and Deep Layers. It is interesting to note that the heating profile is primarily determined by IR heating below 10 km, while both solar and IR contribute nearly equally in the 10–12 km range, and solar heating dominates above. The cloud radiative heating in the midtroposphere is small compared to the latent heating found at these levels [*Schumacher et al.*, 2004]. In the upper troposphere, however, there is little latent heating; therefore, the cloud radiative heating due to cirrus becomes relatively more important.
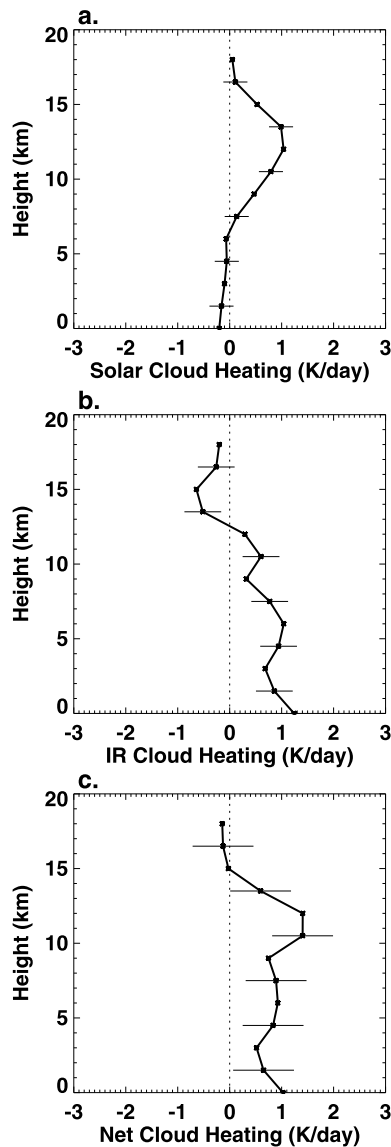
Figure 10. (a) Solar, (b) IR, and (c) Net cloud heating rates with uncertainty estimates (bars) for Southeast Asia.

Table 2 summarizes the statistics of the solar, infrared, and net cloud radiative effect for each cloud type at the TOA, the atmosphere as a whole (ATM), and the surface (SFC). The cloud radiative effect is defined as the difference between the clear-sky and the all-sky radiative fluxes. These statistics are derived from twice-daily observations at approximately 0130 and 1330 local time; such that approximately half of the solar cloud radiative effects values are zero. It is also important to note that we make no correction for diurnal cycle in the A-Train observations.

Cirrus, on average, are relatively transparent to solar radiation, reflecting a small amount of incoming solar radiation, and in the IR, cirrus significantly reduce the amount of outgoing longwave radiation, such that the net cloud radiative effect can be positive depending on their optical thickness. We find that the positive net cloud radiative effect increases with increasing IWP from TTL Cirrus, to Thin Cirrus, to Thick Cirrus (Table 2). Since the Deep Layers are optically thick, they reflect a large amount of incoming solar radiation, creating a strong solar cooling at the SFC. However, these Deep Layers are effectively opaque in the IR, absorbing much of the outgoing IR radiation in the atmosphere thereby creating a significant ATM warming. As such, the Deep Layers are most efficient at reducing the incoming solar and outgoing longwave radiation compared to the other cloud types. These effects partially cancel and the net effect is significant cooling at the TOA due to Deep Layers. The Midlevel Clouds primarily cool the SFC, warm the ATM, and have a near neutral cloud radiative effect at the TOA. Low-Level Clouds, owing to their high albedo, have a strong cooling effect at the SFC which is uncompensated by IR effects at the TOA.

The Deep Layers, which likely consist of stratiform rain with embedded deep convection, are an integral part of the radiation budget in this monsoon region and tend to shield the SFC from sunlight but warm the ATM with a net negative CRE at TOA. The other cloud type that is critical to the radiation budget of this region is cirrus. In comparison to the Deep Layers, the cirrus cloud types occur more frequently and produce a modest warming effect at the TOA that is realized primarily by heating in the ATM partially compensated for by SFC cooling. The net radiative effect of these cloud types results in a broad distribution of cloud radiative effect at the TOA, with values ranging from $-500\,\mathrm{W\,m^{-2}}$ (cooling) to $+200\,\mathrm{W\,m^{-2}}$ (warming), as shown in Figure 11a. The mean and median values ($-23\,\mathrm{W\,m^{-2}}$ and $20\,\mathrm{W\,m^{-2}}$, respectively), however, are both very nearly zero relative to the distribution. This near balance in the net TOA radiation budget during the monsoon season is achieved due to the compensating effects of Deep Layers and cirrus. This offset between optically thin and optically thick clouds in deep convective complexes was also noted by *Hartmann et al.* [2001]. Our results are consistent with their finding that the small net radiative flux at the TOA is not a property of a single cloud type, but rather is due to the ensemble of clouds produced in convectively active regions in the tropics.

Comparing the cloud radiative effect at the TOA with how those effects are distributed between the ATM and SFC (Figures 11b and 11c) show the decoupling between the TOA and SFC radiative budgets noted by *Stephens and Webster* [1984]. Even though the TOA cloud radiative effect is approximately neutral, that

BERRY AND MACE 9503

Table 2. Statistics of Shortwave, Longwave, and Net Cloud Radiative Effect for Each Cloud Type at the Top of the Atmosphere, Atmosphere, and Surface[a]

|		Solar CRE (W m^{-2})			IR CRE (W m^{-2})			Net CRE (W m^{-2})		
		Median	Mean	SD	Median	Mean	SD	Median	Mean	SD
TTL Cirrus	TOA	−5 (−10)	**−30**	88	20	**35**	38	10	**5**	84
	ATM	0 (1)	6	22	10	29	40	20	35	43
	SFC	−5 (−10)	−36	107	0	6	14	−5	−30	100
Thin Cirrus	TOA	−2 (−30)	**−27**	76	30	**41**	35	20	**14**	77
	ATM	0 (1)	6	20	30	36	36	30	42	40
	SFC	−2 (−40)	−34	96	0	5	12	−2	−28	88
Thick Cirrus	TOA	−10 (−80)	**−59**	96	80	**88**	45	30	**29**	84
	ATM	0 (10)	8	17	70	80	45	90	89	50
	SFC	−10 (−100)	−67	109	5	8	11	−10	−59	107
Deep Layers	TOA	0 (−500)	**−209**	265	150	**131**	33	60	**−75**	248
	ATM	0 (40)	23	32	100	109	33	150	133	46
	SFC	0 (−500)	−232	288	20	22	12	2	−211	289
Midlevel	TOA	0 (−60)	**−61**	125	60	**58**	21	40	**−4**	123
	ATM	0 (30)	22	40	40	33	20	40	56	44
	SFC	0 (−150)	−84	161	20	24	15	5	−60	158
Low	TOA	−10 (−100)	**−88**	146	20	**22**	14	5	**−67**	147
	ATM	10 (40)	27	39	−15	−9	19	10	18	43
	SFC	−40 (−150)	−117	180	30	31	13	−15	−85	178

[a]The median, mean, and standard deviation are noted for each distribution. For the solar cloud radiative effects we also include the median daytime value in parenthesis. Bold numbers are the mean values of solar, infrared, and net cloud radiative effects at the TOA.

neutrality is realized by strong solar cooling at the SFC and IR heating in the ATM. Clearly, this decoupling has strong implications for convection since it would tend to stabilize the atmosphere given the tendency for the ATM heating to be realized in the upper troposphere.

We return finally to the role of cirrus in the tropical upper troposphere. As shown, the radiative heating by these hydrometeor layers appear to be fundamental to the energy budget of the tropical atmosphere in this monsoon region (and likely elsewhere). Because the radiative effects of tropical high clouds are expected to become more positive as climate warms, the positive feedback by tropical cirrus is expected to amplify anthropogenic climate change. Obviously cirrus in the tropical upper troposphere are quite varied and understanding how heating in the upper troposphere is distributed across the cirrus continuum is important in understanding what processes must be captured well in models for this feedback to be faithfully rendered in simulations. Most past studies have focused on the portion of the cirrus continuum that would typically be represented by the thickest fraction of these layers where most of the mass is contained. Given our analysis, it is not obvious that this focus is justified.

To determine how the cirrus TOA cloud radiative effect varies depending on the cloud macrophysical properties, we examine the solar, IR, and net cloud radiative effects as mean values in IWP bins, shown in Figure 12b. Overall, there is a positive net cloud radiative effect for IWP values less than $200 \, g \, m^{-2}$. With increasing IWP, the mean TOA net cloud radiative effect increases to a peak value of $50 \, W \, m^{-2}$ at an IWP of $40 \, g \, m^{-2}$. For IWP less than $40 \, g \, m^{-2}$, cirrus significantly reduce the outgoing longwave radiation, while having a smaller effect on solar radiation, a relationship that was illustrated by *Ackerman et al.* [1988]. We find that for IWP less than $40 \, g \, m^{-2}$, the LW cloud radiative effect dominates and leads to an increasingly positive net cloud radiative effects with increasing IWP. Between 40 and $200 \, g \, m^{-2}$, the mean TOA net cloud radiative effect remains positive, but decreases with increasing IWP. It is in this range of IWP (40–$200 \, g \, m^{-2}$) that the solar cloud radiative effect becomes increasingly important for the net cloud radiative effect. At IWP values greater than $200 \, g \, m^{-2}$, reflected solar radiation continues to increase with increasing IWP, while the LW cloud radiative forcing remains constant, an effect that was described by *Stephens and Webster* [1981]. For IWP greater than $200 \, g \, m^{-2}$, the solar cloud radiative effect dominates and leads to an increasingly negative net cloud radiative effect with increasing IWP.

To determine which cirrus contribute most to heating the upper troposphere, we weight the mean TOA net cloud radiative effect as a function of IWP in Figure 12b by the frequency of occurrence for each given IWP bin in Figure 12a. Hence, if a given IWP has a strong TOA net cloud radiative effect but occurs rarely, it will not have a large impact on the overall TOA net cloud radiative effect. The mean net cloud radiative effect at the
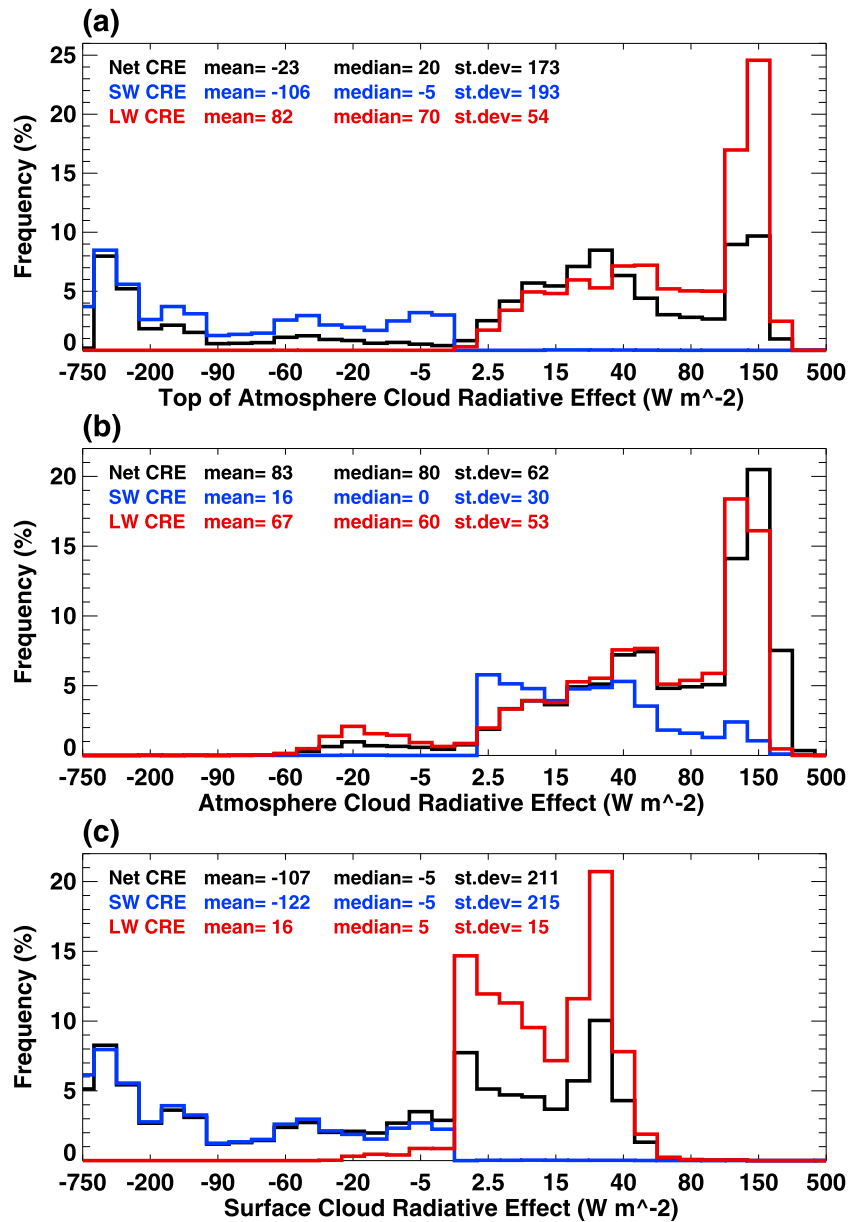
Figure 11. The distribution of cloud radiative properties (a) at the top of the atmosphere, (b) within the atmosphere, and (c) at the surface during the Southeast Asia monsoon season. The net cloud radiative effects are plotted in black, the daytime shortwave cloud radiative effects are plotted in blue, and the longwave cloud radiative effects are plotted in red. For each level, the mean, median, and standard deviation of the cloud radiative effects (including both day and night profiles) are given (in watts per square meter).

TOA for cirrus is $21 \, W \, m^{-2}$ (the sum of the bins in Figure 12c). This analysis reveals that cirrus with an IWP of around $20 \, g \, m^{-2}$, approximately the median IWP, contribute most to the radiative heating in this region, given the TOA net cloud radiative effect (~$40 \, W \, m^{-2}$) and relative frequency of occurrence. Therefore, for models to replicate the radiative heating found in nature, they must accurately simulate the full distribution of IWP but especially the cirrus with IWP in the range of 5 to $60 \, g \, m^{-2}$ where the majority of the radiative effect of cirrus is realized. Diagnostic studies that focus on the mean of the cloud IWP distribution are not informative because the layers that tend to determine the mean IWP do not significantly influence the regional radiation budget and the layers that do influence the regional radiation budget contribute little to the mean IWP. It is also worth noting that the layers that contribute most to the regional radiation budget require both a radar and a lidar for the radiatively important parts of that distribution to be observed fully (Figure 7).
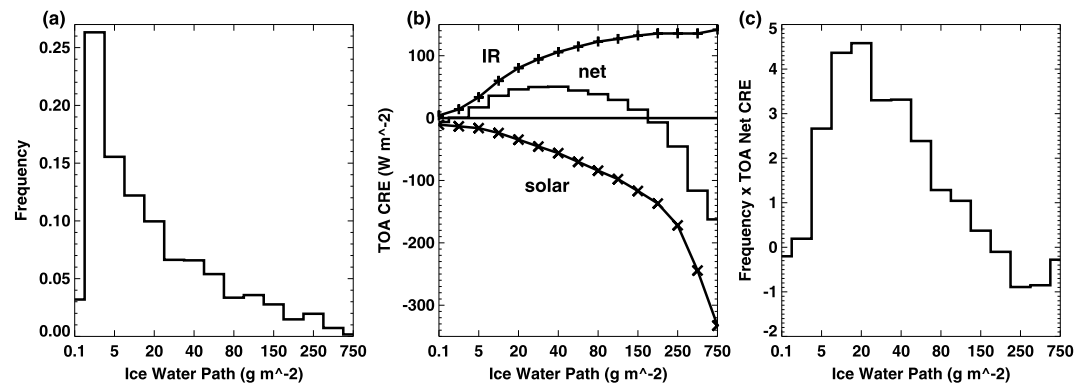
Figure 12. (a) Cirrus (top > 10 km thickness 0–6 km) IWP frequency, mean TOA SW (cross), mean TOA LW (plus), and (b) mean TOA Net cloud radiative effect as a function of IWP and (c) mean TOA net cloud radiative effect weighted by frequency of IWP.

5. Summary and Conclusions

In this study we improve upon an existing A-Train cloud property algorithm [*Mace*, 2010] by incorporating 2C_ICE data [*Deng et al.*, 2010] to examine clouds and their radiative effects in Southeast Asia during two monsoon seasons. Based on the CloudSat radar and CALIPSO lidar, we find that cloud cover in Southeast Asia exceeds 85% during the monsoon months of August–September. The vertical distribution of cloud occurrence frequency reveals that clouds in the upper troposphere are the most prevalent, with a peak exceeding 35% between 10 and 15 km.

We take advantage of the new 2C-ICE CloudSat data product [*Deng et al.*, 2010], which provides ice microphysical properties that are derived using information from both the CloudSat radar and CALIPSO lidar. We find that the mean value of IWP for much of this geographical region is quite large (in excess of 400 g m^{-2}) while the distribution of IWP is strongly skewed and not well described by the mean. We find that the smallest one third of ice water paths values in the distribution are primarily observed by the lidar only, while the largest one third of ice water paths are nearly entirely observed by the radar only, while the middle third of the distribution exploits the maximum synergy between the two instruments highlighting the need for both instruments to fully describe the distribution of ice water path in this convective region.

The mean net cloud radiative heating for Southeast Asia during the monsoon season is positive throughout most of the troposphere with a peak of 1.5 K d^{-1} near 12 km. While all of the solar heating occurs in the upper troposphere (8–16 km), the IR in contrast is characterized by cooling at cloud top (13–17 km) and warming lower in the atmosphere, with a peak of 1.1 K d^{-1} at 6 km.

The distribution of net cloud radiative effects at the TOA spans a large range of values from −500 W m^{-2} to +200 W m^{-2}, with maxima in the distribution indicating a dependence on different cloud types. Given the extremes in cloud radiative effect and the broad distribution of TOA radiative effects, the near cancellation of CRE at the TOA is noteworthy. However, this balance is largely due to a cancellation by surface cooling due to optically thick layers that shield the surface from sunlight and cirrus that warm the atmosphere through IR absorption. In the atmosphere, clouds have a positive forcing in both the SW and LW, leading to a warming with a mean net cloud radiative effect of 83 W m^{-2}. At the surface we find that clouds have a strong negative SW forcing (during the day) and a weakly positive IR forcing, leading to a cooling effect (mean net CRE = −107 W m^{-2}) by clouds at the surface. This distribution of cooling at the surface and heating in the upper troposphere can have a decided influence on atmospheric stability and therefore convection [i.e., *Ramanathan and Collins*, 1991].

Given the critical role that cirrus play in the heat balance of the tropical atmosphere and their role in climate change feedbacks, we examined how the cirrus radiative effects are distributed as a function of macrophysical cloud properties. The mean net cloud radiative effect at the TOA due to cirrus layers is a warming of 21 W m^{-2}, but varies as a function of IWP. The mean net cloud radiative effect at the TOA as a function of cirrus IWP increases from near zero for tenuous TTL cirrus up to a peak of 40 W m^{-2} in the IWP

range of 20 to 60 g m^{-2}. The cirrus cloud radiative effect then decreases with increasing IWP to 0 W m^{-2} at an IWP of 200 g m^{-2}, beyond which the mean net cloud radiative effect at the TOA becomes increasingly negative for larger IWP. By weighting the CRE-IWP distribution by the frequency of occurrence of IWP we diagnose the relative contribution to the TOA cloud radiative effect of cirrus as a function of IWP. We find that cirrus with IWP between 5 and 60 g m^{-2} with a peak at approximately 20 g m^{-2} contribute the most to heating at the TOA.

There are two relevant points that we make based on these results. First, from an observational perspective, the combination of the radar and lidar reach their maximum degree of synergy in the IWP range where the occurrence-weighted cloud radiative effect distribution peaks. Second, we emphasize that the highly skewed distribution of IWP in these convective regions makes the mean value of IWP a particularly poor diagnostic with which to compare models and measurements. Not only does the mean IWP fail to capture the nature of the IWP distribution, the value of the mean IWP is decoupled from the important radiative effects of these clouds. We note the consensus among GCMs to produce a positive feedback due to high clouds, despite their factor of 5 differences in global mean cloud IWP. This apparent insensitivity of the feedback to the disparity in global mean cloud IWP will be a topic of our ongoing research.

References

Ackerman, T. P., K.-N. Liou, F. P. J. Valero, and L. Pfister (1988), Heating rates in tropical anvils, *J. Atmos. Sci.*, *45*, 1606–1623.

Andrews, T., J. M. Gregory, M. J. Webb, and K. E. Taylor (2012), Forcing, feedbacks and climate sensitivity in CMIP5 coupled atmosphere-ocean climate models, *Geophys. Res. Lett.*, *39*, L09712, doi:10.1029/2012GL051607.

Austin, R. T., A. J. Heymsfield, and G. L. Stephens (2009), Retrieval of ice cloud microphysical parameters using the CloudSat millimeter-wave radar and temperature, *J. Geophys. Res.*, *114*, D00A23, doi:10.1029/2008JD010049.

Cetrone, J., and R. A. Houze Jr. (2009), Anvil clouds in tropical mesoscale convective systems in monsoon regions, *Q. J. R. Meteorol. Soc.*, *135*, 305–317, doi:10.1002/qj.389.

Chen, T., W. B. Rossow, and Y. Zhang (2000), Radiative effects of cloud-type variations, *J. Clim.*, *13*, 264–286.

Deng, M., G. G. Mace, Z. Wang, and H. Okamoto (2010), Tropical Composition, Cloud and Climate Coupling Experiment validation for cirrus cloud profiling retrieval using CloudSat radar and CALIPSO lidar, *J. Geophys. Res.*, *115*, D00J15, doi:10.1029/2009JD013104.

Deng, M., G. G. Mace, Z. Wang, and P. Lawson (2013), Evaluation of several A-Train ice cloud retrieval products with in situ measurements collected during the SPartICus campaign, *J. Appl. Meteorol. Climatol.*, *52*, 1014–1030.

Eliasson, S., S. A. Buehler, M. Milz, P. Ericsson, and V. O. John (2011), Assessing observed and modeled spatial distributions of ice water path using satellite data, *Atmos. Chem. Phys.*, *11*, 375–391.

Fu, Q. (1996), An accurate parameterization of the solar radiative properties of cirrus clouds for climate models, *J. Clim.*, *9*, 2058–2082.

Fu, Q., P. Yang, and W. B. Sun (1998), An accurate parameterization of the infrared radiative properties of cirrus clouds for climate models, *J. Clim.*, *9*, 2223–2237.

Hartmann, D. L., L. A. Moy, and Q. Fu (2001), Tropical convection and the energy balance at the top of the atmosphere, *J. Clim.*, *14*, 4495–4511.

Haynes, J. M., T. H. Vonder Harr, T. L'Ecuyer, and D. Henderson (2013), Radiative heating characteristics of Earth's cloudy atmosphere from vertically resolved active sensors, *Geophys. Res. Lett.*, *40*, 624–630, doi:10.1002/grl.50145.

Henderson, D. S., T. L'Ecuyer, G. Stephens, P. Partain, and M. Sekiguchi (2013), A multisensor perspective on the radiative impacts of clouds and aerosols, *J. Appl. Meteorol. Climatol.*, *52*, 853–871.

Houze, R. A., and D. D. Churchill (1987), Mesoscale organization and cloud microphysics in a Bay of Bengal depression, *J. Atmos. Sci.*, *44*, 1845–1867.

Houze, R. A., D. C. Wilton, and B. F. Smull (2007), Monsoon convection in the Himalayan region as seen by TRMM precipitation radar, *Q. J. R. Meteorol. Soc.*, *133*, 1389–1411.

Hoyos, C. D., and P. J. Webster (2007), The role of intraseasonal variability in the nature of Asian monsoon precipitation, *J. Clim.*, *20*, 4402–4424.

Im, E., S. L. Durden, and C. Wu (2006), Cloud Profiling Radar for the CloudSat mission, *IEEE Aerosp. Electron. Syst. Mag.*, *20*, 15–18.

Jensen, M. P., and A. D. Del Genio (2003), Radiative and microphysical characteristics of deep convective systems in the tropical Western Pacific, *J. Appl. Meteorol.*, *42*, 1234–1254.

Jiang, J. H., et al. (2012), Evaluation of cloud and water vapor simulations in CMIP5 climate models using NASA "A-Train" satellite observations, *J. Geophys. Res.*, *117*, D14105, doi:10.1029/2011JD017237.

Kato, S., T. P. Ackerman, J. H. Mather, and E. E. Clothiaux (1999), The k-distribution method and correlated-k approximation for a shortwave radiative transfer model, *J. Quant. Spectrosc. Radiat. Transfer*, *62*, 109–121.

Kato, S., G. L. Smith, and H. W. Barker (2001), Gamma-weighted discrete ordinate two-stream approximation for computation of domain-averaged solar irradiance, *J. Atmos. Sci.*, *58*, 3797–3803.

Kiehl, J., J. Hack, G. B. Bonan, B. A. Boville, D. L. Williamson, and P. J. Rasch (1998), The National Center for Atmospheric Research Community Climate Model: CCM3, *J. Clim.*, *11*, 1131–1149.

L'Ecuyer, T. S., and J. H. Jiang (2010), Touring the atmosphere aboard the A-Train, *Phys. Today*, *63*(7), 36–41, doi:10.1063/1.3463626.

L'Ecuyer, T. S., N. B. Wood, T. Haladay, G. L. Stephens, and P. W. Stackhouse Jr. (2008), Impact of clouds on atmospheric heating based on RO4 CloudSat fluxes and heating rates data set, *J. Geophys. Res.*, *113*, D00A15, doi:10.1029/2008JD009951.

Li, J.-L. F., et al. (2012), An observationally based evaluation of cloud ice water in CMIP3 and CMIP5 GCMs and contemporary reanalyses using contemporary satellite data, *J. Geophys. Res.*, *117*, D16105, doi:10.1029/2012JD017640.

Li, J.-L. F., et al. (2013), Characterizing and understanding radiation biases in CMIP3/CMIP5 GCMs, contemporary GCM, and reanalysis, *J. Geophys. Res. Atmos.*, *118*, 8166–8184, doi:10.1002/jgrd.50378.

Mace, G. G. (2010), Cloud properties and radiative forcing over the maritime storm tracks of the North Atlantic and Southern Ocean as derived from A-Train, *J. Geophys. Res.*, *115*, D10201, doi:10.1029/2009JD012517.

Mace, G. G., and S. Benson (2008), The vertical distribution of cloud radiative forcing at the SGP ARM Climate Research Facility as revealed by 8-years of continuous data, *J. Clim.*, *21*, 2591–2610.

Mace, G. G., and Q. Zhang (2014), The CloudSat radar-lidar geometrical profile product (RL-GeoProf): Updates, improvements, and selected results, *J. Geophys. Res. Atmos.*, doi:10.1002/2013JD021374.

Mace, G. G., et al. (2006), Cloud radiative forcing at the ARM Climate Research Facility: 1. Technique, validation, and comparison to satellite-derived diagnostic quantities, *J. Geophys. Res.*, *111*, D11S90, doi:10.1029/2005JD005921.

Mace, G. G., R. Marchand, Q. Zhang, and G. Stephens (2007), Global hydrometeor occurrence as observed by CloudSat: Initial observations from summer 2006, *Geophys. Res. Lett.*, *34*, L09808, doi:10.1029/2006GL029017.

Mace, G. G., Q. Zhang, M. Vaughn, R. Marchand, G. Stephens, C. Trepte, and D. Winker (2009), A description of hydrometeor layer occurrence statistics derived from the first year of merged Cloudsat and CALIPSO data, *J. Geophys. Res.*, *114*, D00A26, doi:10.1029/2007JD009755.

Marchand, R., G. G. Mace, T. Ackerman, and G. Stephens (2008), Hydrometeor detection using Cloudsat—An Earth-orbiting 94-GHz cloud radar, *J. Atmos. Oceanic Technol.*, *25*, 519–533.

Mather, J. H., and S. A. McFarlane (2009), Cloud classes and radiative heating profiles at the Manus and Nauru Atmospheric Radiation Measurement (ARM) sites, *J. Geophys. Res.*, *114*, D19204, doi:10.1029/2009JD011703.

Mather, J. H., S. A. McFarlane, M. A. Miller, and K. L. Johnson (2007), Cloud properties and associated radiative heating rates in the tropical Western Pacific, *J. Geophys. Res.*, *112*, D05201, doi:10.1029/2006JD007555.

McFarlane, S. A., J. H. Mather, and T. P. Ackerman (2007), Analysis of tropical radiative heating profiles: A comparison of models and observations, *J. Geophys. Res.*, *112*, D14218, doi:10.1029/2006JD008290.

Mlawer, E. J., S. J. Taubman, P. D. Brown, M. J. Iacono, and S. A. Clough (1997), Radiative transfer for inhomogeneous atmospheres: RRTM, a validated correlated-k model for the longwave, *J. Geophys. Res.*, *102*, 16,663–16,682, doi:10.1029/97JD00237.

Park, M., W. J. Randel, A. Gettelman, S. T. Massie, and J. H. Jiang (2007), Transport above the Asian summer monsoon anticyclone inferred from Aura Microwave Limb Sounder tracers, *J. Geophys. Res.*, *112*, D16309, doi:10.1029/2006JD008294.

Partain, P. (2004), CloudSat ECMWF-AUX auxiliary data process description and interface control document, Coop. Inst. for Res. in the Atmos., Colo. State Univ., Fort Collins.

Platnick, S., M. D. King, S. A. Ackerman, W. P. Menzel, B. A. Baum, J. C. Riedi, and R. A. Frey (2003), The MODIS cloud products; Algorithms and examples from Terra, *IEEE Trans. Geosci. Remote Sens.*, *21*, 459–473, doi:10.1109/TGRS.2002.808301.

Powell, S., R. A. Houze, A. Kumar, and S. A. McFarlane (2012), Comparison of simulated and observed continental tropical anvil clouds and their radiative heating profiles, *J. Atmos. Sci.*, *69*, 2662–2681.

Protat, A., S. A. Young, S. A. McFarlane, T. L'Ecuyer, G. G. Mace, J. M. Comstock, C. N. Long, E. Berry, and J. Delanoe (2014), Reconciling ground-based and space based estimates of the frequency of occurrence and radiative effect of clouds around Darwin, Australia, *J. Appl. Meteorol. Climatol.*, *53*, 456–478, doi:10.1175/JAMC-D-13-072.1.

Ramanathan, V., and W. Collins (1991), Thermodynamic regulation of ocean warming by cirrus clouds deduced from observations of the 1987 El Niño, *Nature*, *351*, 27–32.

Romatschke, U., and R. A. Houze Jr. (2011), Characteristics of precipitating convective systems in the South Asian Monsoon, *J. Hydrol.*, *12*, 3–26.

Rossow, W. B., and A. A. Lacis (1990), Global, seasonal cloud variations from satellite radiance measurements. Part II: Cloud properties and radiative effects, *J. Clim.*, *3*, 1204–1253.

Schumacher, C., R. A. Houze, and I. Kraucunas (2004), The tropical dynamical response to latent heating estimates derived from the TRMM precipitation radar, *J. Atmos. Sci.*, *61*, 1341–1358.

Schumacher, C., P. E. Ciesielski, and M. H. Zhang (2008), Tropical cloud heating profiles: Analysis from KWAJEX, *Mon. Weather Rev.*, *136*, 4289–4300.

Schwartz, M. C., and G. G. Mace (2010), Co-occurrence statistics of tropical tropopause layer cirrus with lower cloud layers as derived from CloudSat and CALIPSO data, *J. Geophys. Res.*, *115*, D20215, doi:10.1029/2009JD012778.

Slingo, J. M. (1989), A GCM parameterization for the shortwave radiative properties of water clouds, *J. Atmos. Sci.*, *46*, 1419–1427.

Soden, B. J., and G. A. Vecchi (2011), The vertical distribution of cloud feedback in coupled ocean-atmosphere models, *Geophys. Res. Lett.*, *38*, L12704, doi:10.1029/2011GL047632.

Stephens, G. L. (2005), Cloud feedback in the climate system: A critical review, *J. Clim.*, *18*, 237–273.

Stephens, G. L., and P. J. Webster (1981), Clouds and climate: Sensitivity of simple systems, *J. Atmos. Sci.*, *38*, 235–247.

Stephens, G. L., and P. J. Webster (1984), Cloud decoupling of the surface and planetary radiative budgets, *J. Atmos. Sci.*, *41*, 681–686.

Stephens, G. L., et al. (2012), An update on Earth's energy balance in light of the latest global observations, *Nat. Geosci.*, *5*, 691–696, doi:10.1038/NGEO1580.

Su, H., et al. (2013), Diagnosis of regime-dependent cloud simulation errors in CMIP5 models using "A-Train" satellite observations and reanalysis data, *J. Geophys. Res. Atmos.*, *118*, 2762–2780, doi:10.1029/2012JD018575.

Toon, O. B., C. P. McKay, T. P. Ackerman, and K. Santhanam (1989), Rapid calculation of radiative heating rates and photodissociation rates in inhomogeneous multiple scattering atmospheres, *J. Geophys. Res.*, *94*(D13), 16,287–16,301, doi:10.1029/JD094iD13p16287.

Waliser, D. E., et al. (2009), Cloud ice: A climate model challenge with signs and expectations of progress, *J. Geophys. Res.*, *114*, D00A21, doi:10.1029/2008JD010015.

Waliser, D. E., J.-L. F. Li, T. S. L'Ecuyer, and W.-T. Chen (2011), The impact of precipitating ice and snow on the radiative balance in global climate models, *Geophys. Res. Lett.*, *38*, L06802, doi:10.1029/2010GL046478.

Wang, Z., D. Vane, G. Stephens, and D. Reinke (2011), Level 2 combined radar and lidar cloud scenario classification product process description and interface control document, Jet Propul. Lab., Calif. Inst. of Tech., Pasadena.

Wentz, F. J., and T. Meissner (2000), AMSR Algorithm Theoretical Basis Document (ATBD) version 2, AMSR ocean algorithm. RSS Tech. Proposal 121599A-1, 59 pp.

Wielicki, B. A., et al. (1998), Clouds and the Earth's Radiant Energy System (CERES): Algorithm overview, *IEEE Trans. Geosci. Remote Sens.*, *36*(4), 1127–1141.

Winker, D. M., B. H. Hunt, and M. J. McGill (2007), Initial performance assessment of CALIOP, *Geophys. Res. Lett.*, *34*, L19803, doi:10.1029/2007GL030135.

Zelinka, M. D., and D. L. Hartmann (2010), Why is longwave cloud feedback positive?, *J. Geophys. Res.*, *115*, D16117, doi:10.1029/2010JD013817.

Zhang, Y., W. B. Rossow, A. A. Lacis, V. Oinas, and M. I. Mishchenko (2004), Calculation of radiative fluxes from the surface to top of atmosphere on ISCCP and other global data sets: Refinements on the radiative transfer model and the input data, *J. Geophys. Res.*, *109*, D19105, doi:10.1029/2003JD004457.

Zuidema, P. (2003), Convective clouds over the Bay of Bengal, *Mon. Weather Rev.*, *131*, 780–798.